Journal of Biomechanics 172 (2024) 112209

Contents lists available at ScienceDirect

Journal of Biomechanics

journal homepage: www.elsevier.com/locate/jbiomech

Elastic response of trabecular bone under compression calculated using the firm and floppy boundary lattice element method

Mahsa Zojaji [a,b], Keyvan Ferasat [a,1], McKinley Van Klei [a,b], Hao Sun [a], Kail Beloglowka [a,b], Brian Kunath [a,b], Roshni Rainbow [a,b], Heidi-Lynn Ploeg [a,b], Laurent Karim Béland [a,*]

[a] Department of Mechanical and Materials Engineering, Smith Engineering, Queen's University, Kingston, Ontario, Canada
[b] Centre for Health Innovation, Kingston Health Sciences Centre, Queen's University, Kingston, Ontario, Canada

ARTICLE INFO

Keywords:
Finite element analysis
Lattice element method
Bone mechanical properties
Bone mechanical testing

ABSTRACT

Micro-Finite Element analysis (μFEA) has become widely used in biomechanical research as a reliable tool for the prediction of bone mechanical properties within its microstructure such as apparent elastic modulus and strength. However, this method requires substantial computational resources and processing time. Here, we propose a computationally efficient alternative to FEA that can provide an accurate estimation of bone trabecular mechanical properties in a fast and quantitative way. A lattice element method (LEM) framework based on the Large-scale Atomic/Molecular Massively Parallel Simulator (LAMMPS) open-source software package is employed to calculate the elastic response of trabecular bone cores. A novel procedure to handle pore-material boundaries is presented, referred to as the Firm and Floppy Boundary LEM (FFB-LEM). Our FFB-LEM calculations are compared to voxel- and geometry-based FEA benchmarks incorporating bovine and human trabecular bone cores imaged by micro Computed Tomography (μCT). Using 14 computer cores, the apparent elastic modulus calculation of a trabecular bone core from a μCT-based input with FFB-LEM required about 15 min, including conversion of the μCT data into a LAMMPS input file. In contrast, the FEA calculations on the same system including the mesh generation, required approximately 30 and 50 min for voxel- and geometry-based FEA, respectively. There were no statistically significant differences between FFB-LEM and voxel- or geometry-based FEA apparent elastic moduli (+24.3% or +7.41%, and +0.630% or -5.29% differences for bovine and human samples, respectively).

1. Introduction

Finite element analysis (FEA) is the most well-established and reliable method to estimate the stress and strain in complex structures like bone (Taylor et al., 2002; Srirekha et al., 2010; Taylor and Prendergast, 2015). The prevalence of Computed Tomography (CT) in clinics presents the opportunity to leverage CT data for patient-specific diagnoses and treatments (Bott et al., 2023; Dowhanik et al., 2022). Among the clinical guidelines established to assist in fracture risk assessment, image-based computational modeling holds promise to enhance this evaluation (Derikx et al., 2015; Sas et al., 2020). Advancements in imaging technologies have allowed higher fidelity μFEA simulations in clinics (Flaig, 2012; Nishiyama et al., 2013; Keyak, 2001; Müller and Rüegsegger, 1995; van Rietbergen et al., 1995; Liu et al., 2006) with bone-specific FEA solvers capable of managing millions of degrees of freedom (DOF) (van Rietbergen et al., 1996; Adams et al., 2004; Flaig and Arbenz, 2011; Knowles et al., 2021, 2022, https://bonelab.github.io/n88).

Two approaches for high-resolution trabecular μCT FEA meshing are: geometry-based volumetric from the trabecular surface, and voxel-based which converts voxels to hexahedral elements. Knowles et al. found CPU times for a 27.3 million-element μFEA ranged from 3000 s on Linux GPU to 4700 s on Windows GPU at 10^{-6} mm convergence (Knowles et al., 2022). Benca et al. generated voxel-based μFEA of the human femur with approximately 13,000 elements within 30 min and ran the simulations within 27 min of CPU time, and 390MB of memory, with Abaqus (v.6.14, Simulia) on a desktop PC (4 CPUs, 3.4 GHz) (Benca et al., 2019). Despite the speed and automation of voxel-based meshes, these models have sharp corners on their surfaces that cause stress concentrations (Palumbo et al., 2014; Guldberg et al., 1998) and challenges for interfaces, crack propagation, fracture, or bone modeling/remodeling simulations. Additionally, voxel-to-hexahedral conversion must adopt strategies to avoid connectivity loss (Mengoni et al., 2016; van Rietbergen et al., 1995). Smoothing algorithms have been therefore developed for voxel-based μFEA with

* Corresponding author.
E-mail address: laurent.beland@queensu.ca (L.K. Béland).
[1] co-first author.

https://doi.org/10.1016/j.jbiomech.2024.112209
Accepted 24 June 2024
Available online 28 June 2024

more accurate tissue-level stress and strain predictions (Bardyn et al., 2010; Boyd and Müller, 2006). Geometry-based meshes offer smooth surface representation with low discretization error (Sas et al., 2020; Depalle et al., 2013). Derikx et al. reported 8 h to create a case-specific human femur FEA using linear tetrahedrons with 2 mm edge length (Derikx et al., 2012). Gislason et al. reported 7 h of CPU time to simulate (dual-core 3 GHz CPU, Windows 64-bit, 8 GB RAM) a femur with 1.5 million elements (Gislason et al., 2014).

The accuracy and speed of FEA depends on element type (e.g. hexahedral versus tetrahedral), element size, full or reduced integration, and shape function (linear versus quadratic). Overall, hexahedral elements, larger element size, reduced integration point, and linear shape function reduce CPU time up to 20%, but local stress distribution at the trabecular scale is highly influenced by each of those parameters which may lead to discretization, stiffening, and shear locking errors (Depalle et al., 2013). Additional limitations are increased computational time for non-linear FEA. Knowles et al. demonstrated that linear FEAs for 70,000-element models ran under 1 min of CPU time with Faim (MacBook Pro, Inteli9, 8 core, 32 GB RAM) and almost 2 min with Abaqus (Inteli7, 4 core, 32 GB RAM, 8 CPUs). However, nonlinear FEAs took approximately 3 h in Faim and 30 min in Abaqus (Knowles et al., 2021). Thus, a method that can be both accurate and faster than FEA for fracture risk assessment is needed (Pericoli et al., 2021; Du et al., 2014).

Particle-based numerical simulation methods have been proposed as alternatives, including peridynamics (Silling, 2000; Silling et al., 2007; Zhou and Tian, 2021) and the lattice element method (LEM) (Ostoja-Starzewski, 2002). The latter has mostly been employed in civil engineering materials poromechanics (Laubie et al., 2017a,b,c), successfully modeling elastic, plastic, and fracture behavior of porous materials. In particular, LEM can capture complex anisotropic behavior, plastic deformation, and crack propagation when details are considered in the model, with good numerical efficiency (Chen et al., 2016; Meng et al., 2021; Wei et al., 2020; Nikolić et al., 2018a; Laubie et al., 2017b). Recent studies based on the potential of mean force LEM show promising results to simulate crack propagation in heterogeneous structures as well as modeling of building systems with enhanced computational efficiency (Wang et al., 2021; Razi et al., 2023).

In LEM particles are connected by springs to discretize a continuum solid. These particles are referred to as lattice elements because they are arranged on a regular lattice: simple cubic (SC), body-centered cubic (BCC), or face-centered cubic (FCC). The spring constants are chosen to ensure the change in energy generated by applying a strain to a lattice element is rigorously equal to that of a continuous elastic solid under the same applied strain (Ostoja-Starzewski, 2002). Historically, LEM models were limited to materials with Poisson's ratio of less than 0.25 (Nikolić et al., 2018b). In the last decade, Chen et al. formulated a LEM capable of describing isotropic materials with arbitrary Poisson's ratio by adding a nonlocal parameter to the interparticle interactions (Lin et al., 2015; Chen and Liu, 2016). This nonlocal term can be viewed as an energy penalty for changing the volume of a lattice element. This LEM model was recently implemented using a Large-scale Atomic/Molecular Massively Parallel Simulator (LAMMPS) open-source software package (Thompson et al., 2022; Sun et al., 2022). Of note, the boundary between pores and the solid phase during LEM simulations must be handled with care, as particles at the boundary are under-coordinated (particles with some broken bonds), which can lead to an undesirable characteristic energy response to strain as compared to the fully bonded particles (Nikolic and Ibrahimbegovic, 2015).

In this study, LAMMPS-LEM is proposed as an alternative to FEA to estimate the elastic response of trabecular bone tissue under compression. We compare the bone cores' apparent elastic moduli (E_{app}) predicted by geometry-based and voxel-based FEA, and LAMMPS-LEM simulations and the computational times of these numerical methods.

2. Methods

2.1. Sample preparation

Sixteen human trabecular bone cores (5 mm high by 10 mm diameter) from a previous study were obtained from femoral heads donated by two hip arthroplasty patients (48-year-old male, n = 8; and, 68-year-old female, n = 8, Meyer (2016)), and seventeen bovine trabecular bone cores (10 mm high by 10 mm diameter) with no known diseases were obtained (Kunath et al., 2024). No information on age and sex of the animal was available. Human and bovine bone cores were μCT scanned (Vector4CT, 50 kV, 0.43 mA, 100 ms exposure time, 0.1-degree rotation step in 360°, 20 μm resolution). All μCT data were segmented (Mimics, v23.0, Materialise) using global thresholding (200–5600 Hounsfield Units) and region growing with embedded "six-pixel-connectivity" to remove floating pixels. The bone volume fraction (BV/TV) was assessed for all samples. All numerical methods used the same segmented dataset.

2.2. Geometry-based finite element analysis

The 3D surface mesh from 3-Matic (v16.0, Materialise) closely modeled the trabecular structure with as few triangles as possible to decrease computational time of the FEA solver (Beloglowka, 2022). Triangle reduction was achieved by maintaining a quality of 0.85 (interior angles between 50° to 70°) and a geometrical error of 1.25 μm (maximum deviation from original surface). The resulting surface models (STL ASCII) were imported into Abaqus (v2017, Simulia). All samples were meshed with quadratic tetrahedrons (Fig. 1b and f). The average element and node counts were 3,753,531 ± 701,789, and 6,076,259 ± 1,080,655 for bovine, and 3,022,381 ± 2,136,220, and 4,654,253 ± 3,075,094 for human bone cores. To mimic quasi-static uniaxial compression testing, nodes on lower cylindrical face were fixed in the axial direction (z-axis) while quasi-static uniaxial compression of 4000 $\mu\epsilon$ (axial displacement according to individual core length) was applied to nodes of upper face. Linear-elastic, isotropic, and homogeneous mechanical properties (tissue modulus, E_i = 1 GPa, Poisson's ratio of 0.3) were assumed (same for all numerical methods). For all numerical methods, Hooke's Law was assumed to find E_{app} (Eq. (1)).

$$E_{app} = \frac{KL}{A} \tag{1}$$

where K ($\frac{N}{mm}$) is the reaction force over the applied displacement; L (mm) is the length of the bone core, and A (mm^2) is the bone core cross-sectional area.

2.3. Voxel-based finite element analysis

Segmented μCT data were exported from Mimics as binarized image files, converted to MHA format files (ImageJ, v2, Free Software Foundation Inc.) and imported into an open-source FEA model generator (n88modelgenerator, v9.0, Numerics88 Solutions Ltd) for voxel-based mesh generation (Fig. 1d and h). FEA was performed using an open-source solver, Faim (v8.0, Numerics88 Inc.). A normal compression strain of 4000 $\mu\epsilon$ was applied on nodes of upper cylindrical face and nodes on lower face were fixed in z-axis. Average element and node counts were 24,253,819 ± 3,947,086 and 28,850,935 ± 4,427,805 for bovine and 8,352,461 ± 3,686,904 and 9,898,997 ± 3,405,614 for human bone cores.

2.4. Lattice element method simulations

Lattice element method simulations were carried out with the open-source LAMMPS-LEM package. In this section, a strategy to obtain the LEM parameters and the procedure for preparing input files from μCT data based on the firm and floppy boundary (FFB) method are presented. FFB method is a novel idea for accelerating LAMMPS-LEM calculations.

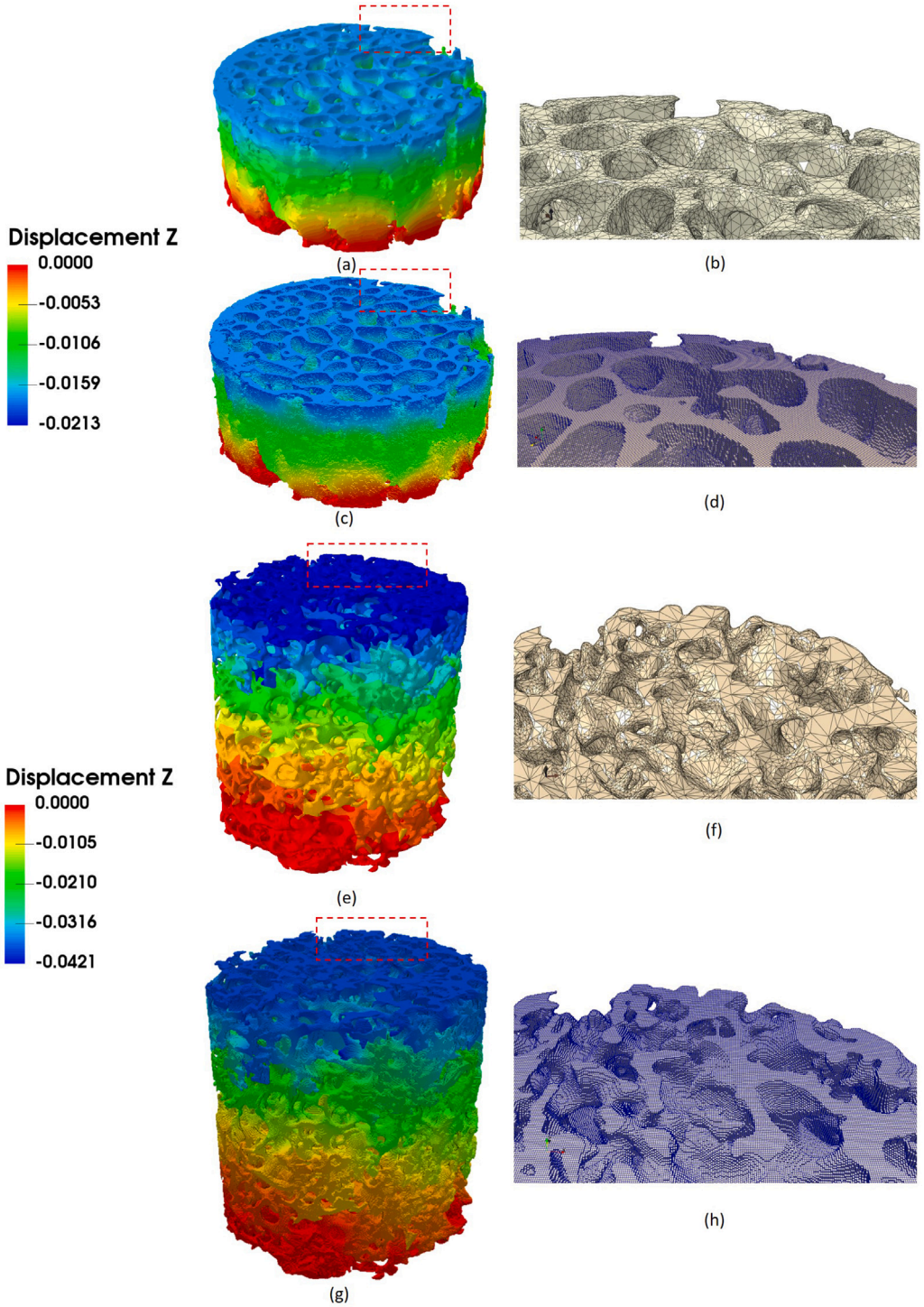

Fig. 1. The μCT-based FEA results of a human and bovine bone cores show the axial displacement (z-axis) magnitude; **a** and **e**: Geometry-based mesh generated FE model of human (3,160,073 elements, 4,525,501 million nodes) and bovine (3,015,073 elements, 4,940,200 nodes) bone cores; **c** and **g**: voxel-based mesh generated FE model of human (4,403,537 elements, 6,009,313 nodes) and bovine (19,636,792 elements, 23,889,513 nodes), respectively; **b** and **f** show the 10-noded tetrahedral mesh on human and bovine FE models for the area bounded by the red dashed-line box; **d** and **h**: 8-noded hexahedral mesh on the human and bovine FE models for the area bounded by the red dashed-line box, respectively.

2.4.1. Parameters in lattice element method

To simulate the desired Poisson's ratio, a nonlocal parameter is defined in addition to the local one for each unit cell, i.e. the spring constant. A unit cell is defined as the closed volume by the middle planes between the particles. Therefore, the number of unit cells is equal to the total number of particles. The total energy ($U_i^{\text{unit cell}}$) for each unit cell (i) is the summation of local (U_i^{local}) and nonlocal (U_i^{nonlocal}) energy terms (Eqs. (3)–(5)).

$$U^{\text{total}} = \sum_{i=1}^{N_t} U_i^{\text{unit cell}} \tag{2}$$

$$U_i^{\text{unit cell}} = U_i^{\text{local}} + U_i^{\text{nonlocal}} \tag{3}$$

$$U_i^{local} = \frac{1}{2} k_i \sum_{j=1}^{N_i} (\delta l_{ij})^2 \quad (4)$$

$$U_i^{nonlocal} = \frac{1}{2} T_i (\sum_{j=1}^{N_i} \delta l_{ij})^2 \quad (5)$$

where U^{total} and N_t are the total energy and number of unit cells/particles in the simulation box. k_i and T_i are respectively the local (pairwise) and nonlocal stiffness parameters. N_i indicates the total number of nearest neighbors (first and second nearest neighbors) which is 18, 14, and 18 for SC, BCC, and FCC structures, respectively. δl_{ij} is half of spring elongation between particles i and j. The stiffness parameters are related to elastic constants and can be calculated as follows for a SC lattice structure, and isotropic material (Eqs. (6)–(7)). For further information on the equations and other crystal structures (BCC and FCC), the readers are referred to (Chen and Liu, 2016).

$$k_1 = k_2 = \frac{(LP)(E)}{1+\nu} \quad (6)$$

$$T = \frac{(LP)(E)(4\nu - 1)}{18(1+\nu)(1-2\nu)}, \quad (7)$$

where k_1 and k_2 are the local stiffness parameters for the bond between the particle and its first and second nearest neighbors. SC has 6 and 12 first and second nearest neighbors, respectively. k_1 and k_2 are equal to each other in SC structures. For BCC and FCC structures, the first and second nearest neighbors local stiffness parameters are not the same (Chen and Liu, 2016; Sun et al., 2022). T is the nonlocal stiffness parameter that allows for a range of Poisson's ratio ($\nu = -1$ to 0.5). E and LP are elastic modulus and lattice parameter, respectively. For convergence analysis, four different lattice parameters (0.06, 0.08, 0.10, and 0.12 mm) were considered.

All of these equations have been implemented in LAMMPS (Sun et al., 2022). To speed up the calculations for porous structures like trabecular bone, we propose a new scheme, FFB method, as explained in the next section. All three SC, BCC, and FCC structures are cubic. SC is identical to voxels, and BCC and FCC are extensions of SC structure. Therefore, these cubic structures represent the trabecular geometry as well as voxel-based meshes.

2.4.2. Firm and floppy boundary method

The main idea of FFB method is that instead of running a resource-intensive simulation with a small lattice parameter, one can run two faster simulations with larger lattice parameters and average those simulations to obtain the final result. Running two separate simulations required two different input configurations, one for each of the firm and floppy boundaries.

A custom-made C code was written to generate input configurations based on segmented μCT data from Mimics. Bonds were inserted between particles using LAMMPS. FFB method was employed to define the bone-pore boundary (Fig. 2). The firm boundary (Figs. 2a & b) interface was "padded" with lattice points, which were not themselves included when calculating stress, but ensured that the boundary lattice sites had full coordination numbers. The firm boundary approach, had no broken bonds on the surface; and therefore, overestimated E_{app}. This approach required a post-processing step using OVITO (v2.9.0) software package to narrow the stress calculation for the sites with the full coordination number (18 bonds for SC and 14 bonds for BCC) (Stukowski, 2009). The floppy boundary (Fig. 2c & d) had no padding; and therefore, all lattice points were included when calculating stress. Boundary lattice particles were not fully coordinated as fewer springs countered their displacement; and therefore, referred to as floppy. Contrary to firm, the floppy boundary method underestimated E_{app} due to floppy bonds on and close to the surface. Final E_{app} was obtained by averaging the firm and floppy boundary methods. The overestimated and underestimated terms come from the divergence of firm and floppy boundary results as the lattice parameter increases from 0.06 mm to 0.12 mm.

LAMMPS-LEM input files were created from the segmented μCT data by executing the custom-made C code twice, one for each of the firm and floppy boundaries (Fig. 2a & c). C code input variables were crystal structure (SC, BCC or FCC) and LP. Multiple input files are created simultaneously with various LPs in one run: 1-fold, 2-fold, 4-fold, 10-fold, and 12-fold of input LP. The segmented μCT data had a SC structure with LP 0.02 mm (voxel size 0.02 mm). In the following, as an example, the steps to build the input file for FBB method are explained for LP 0.12 mm:

1. **Firm boundary method:** Define the input LP as 0.12 mm and use the 1-fold LP output from C code as the input file for simulations. In this case, the particles cover more volume as compared to the segmented μCT data (Fig. 2b)

2. **Floppy boundary method:** Define the input lattice parameter as 0.01 mm and use the 12-fold LP output file. The 12-fold LP is built based on the 1-fold LP (0.01 mm) by deleting some additional particles and keeping the structure similar. Starting with 0.01 mm LP ensures a volume close to the segmented μCT data and maintaining the volume when deleting the particles to get 12-fold LP (Fig. 2d).

The LAMMPS-LEM simulations were run for both firm and floppy boundaries (explained for the LP 0.12 mm of human bone cores):

1. Create bonds and define k_1, k_2, and T parameters (E = 1 GPa, ν = 0.3, LP = 0.12 mm).

2. 0.6 mm of both cylindrical faces were fixed with "setforce" command in LAMMPS to make the force zero in the axial (z-axis) direction and not alter the force in other (x- and y-axis) directions.

3. Both cylindrical faces were displaced by 0.0015 mm, and the system was minimized by the conjugate gradient method. 0.003 mm displacement was applied for bovine bone cores since they were double the length of the human bone cores.

4. Step 3 was repeated seven times for a total displacement of 0.021 mm (strain 4200 $\mu\varepsilon$). Constant displacement increments were defined as they are easier to implement in LAMMPS than constant strain.

For the floppy boundary, the stress was directly extracted from the LAMMPS output file. For the firm boundary, a post-processing step in OVITO (v2.9.0) limited the stress calculations to the fully coordinated particles (red particles in Fig. 2a). The firm boundary E_{app} was found from the summation of stress components for red particles in the axial (z-axis) direction. Finally, the FFB E_{app} was calculated as the average E_{app} of firm and floppy boundary methods. Throughout the remainder of the manuscript, LEM refers to FFB LAMMPS-LEM with SC lattice structure unless otherwise noted.

2.5. Statistical analysis

Linear regressions were performed to assess possible correlations among the different studied parameters (Python v.3.11). Student t-test determined if the slope and intercept of the regression line were significantly different from 0. LEM results were compared to voxel- and geometry-based FEA. Voxel-based was the assumed gold standard for comparisons of FEAs. One-way repeated measures ANOVA tested for differences in E_{app} (α = 0.05, Origin 2023b, student version). Agreement between FEA and LEM results was analyzed with Bland-Altman plots (Bland and Altman, 1986; Giavarina, 2015).

3. Results

3.1. Comparison of LAMMPS-LEM and FEA

Bovine bone cores had a BV/TV range of 22%–38%, and human bone cores BV/TV range was 9%–43%. FEA BV was highly correlated to BV of the segmented μCT data (Fig. 3). The BV of the voxel- and geometry-based FEAs deviated less than 10% from the μCT BV.

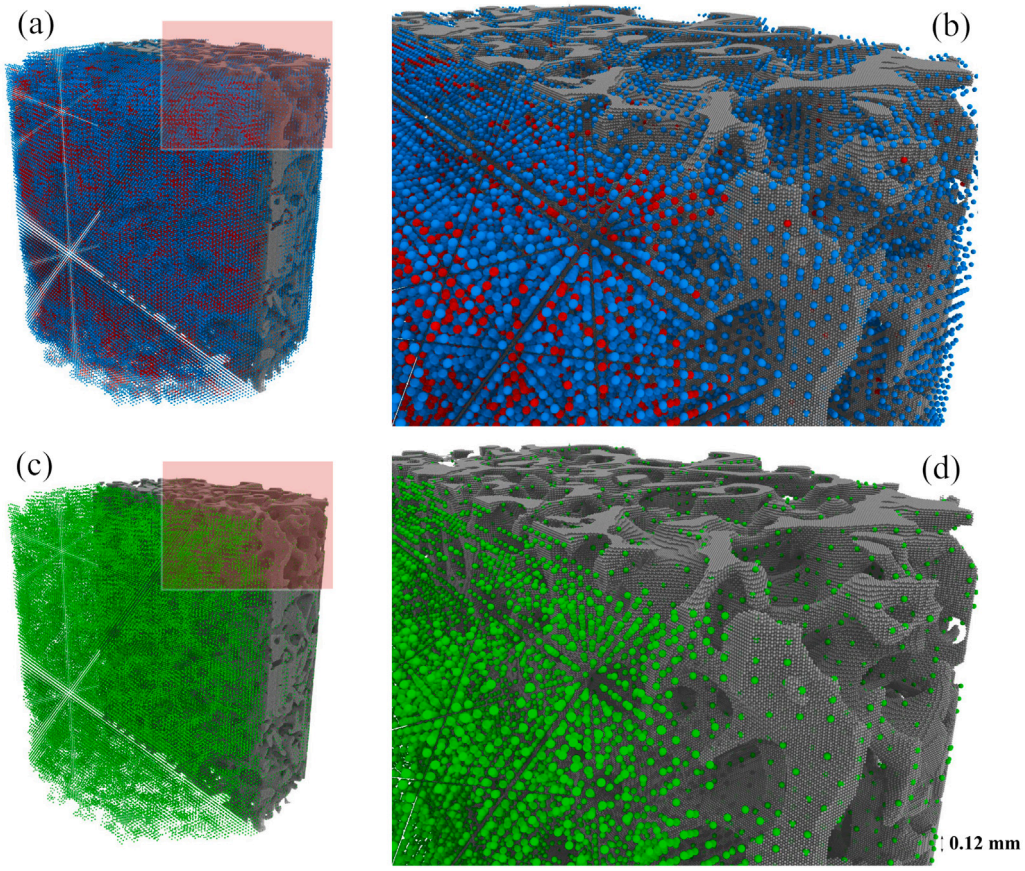

Fig. 2. 3D illustration of a segmented μCT scan of a bovine trabecular bone core (fine gray particles) as obtained using Mimics. **a** and **c** show the firm and floppy boundary particles on top of the fine gray particles, respectively. **b**: The particle lattice corresponding to a firm boundary (large blue particles) is overlaid on top of the segmented μCT data (fine gray particles). The large red particles correspond to fully coordinated particles. **d**: The particle lattice corresponding to a floppy boundary (green particles) is overlaid on top of the segmented data (fine gray particles). The lattice parameter (distance between firm and floppy particles) is 0.12 mm as shown. A 2D illustration of firm and floppy boundary LEM is shown in the supplementary material. (For interpretation of the references to color in this figure legend, the reader is referred to the web version of this article.)

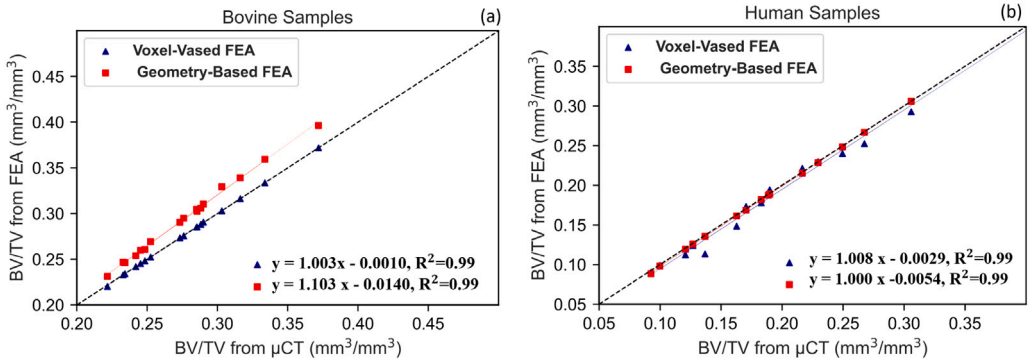

Fig. 3. Regression analysis comparing BV from the original segmented mask with the voxel- and geometry-based models (the equations of the regression lines (y = mx + b) with slopes (regression coefficients, m) and y-intercepts (b), and the coefficients of determination (R^2) are presented (α = 0.05, slope p-value < 0.001)).

The mean percent differences between LEM and voxel or geometry-based FEA predictions were +24.5% or +7.41% for bovine and −3.55% or −5.29% for human bone cores, respectively. The comparison between voxel- and geometry-based FEA found percent differences in E_{app} of −12.8% and −4.38% for bovine and human samples, respectively (Fig. 4a&b). LEM and voxel-based FEA predictions of E_{app} were well correlated for bovine (R^2 = 0.95, slope = 1.25, slope p-value < 0.001, intercept = -0.66, intercept p-value = 0.45) and human bone cores (R^2 = 0.97, slope = 0.97, slope p-value < 0.001, intercept = -0.45, intercept *p*-value = 0.55). The LEM and geometry-based FEA predictions of E_{app} also exhibited strong correlations. For bovine, the R^2 was 0.92, with a slope of 1.03 (p-value < 0.001), and for human bone cores, the R^2 was 0.93, with a slope of 0.93 (p-value < 0.001) (Fig. 4c&d).

All three methods could estimate the effect of bone topology on its mechanical properties, beyond the effect of BV/TV. In general, the E_{app} normalized for BV/TV as predicted by all three methods were in good agreement. For bovine trabecular bone cores, LEM E_{app} normalized to BV/TV was highly correlated with the voxel-based FEA (R^2 = 0.96, slope p-value < 0.001). A moderate correlation was found between LEM and geometry-based FEA normalized to BV/TV (R^2 = 0.55, slope p-value < 0.001) (Fig. 5a). For human trabecular bone cores, LEM E_{app}

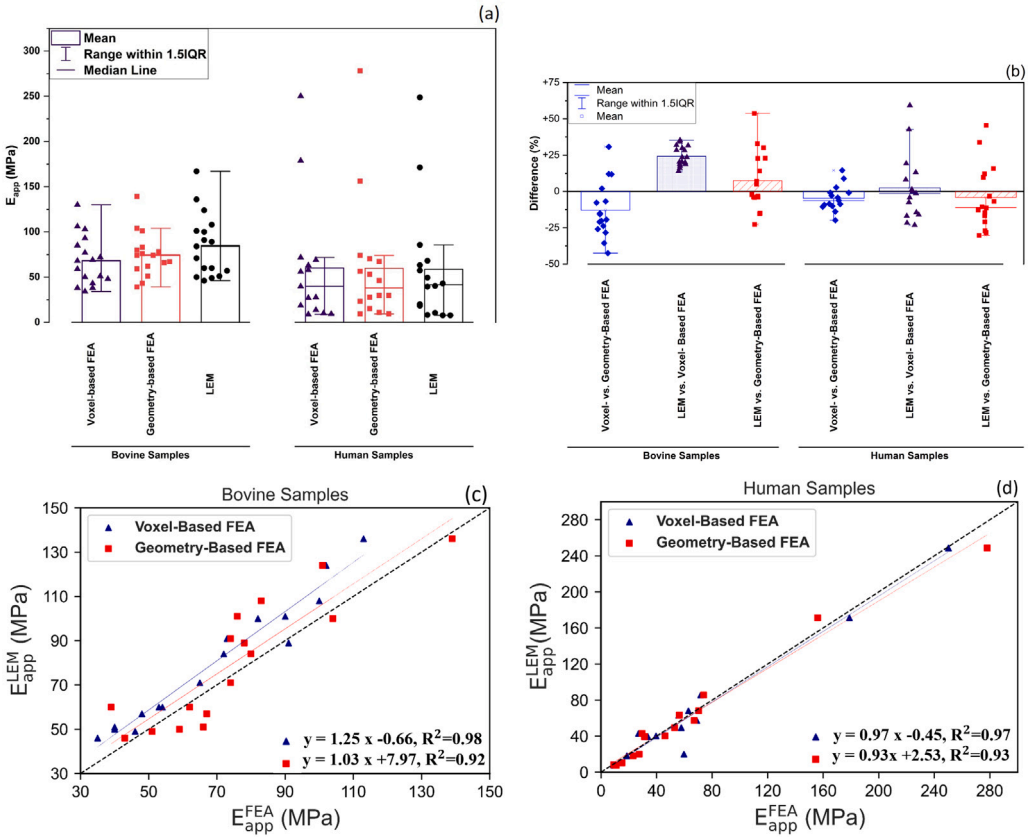

Fig. 4. **(a)** Bar-whisker plot of E_{app} of the bovine and human trabecular bone cores predicted using voxel-based FEA, geometry-based FEA, and LEM. **(b)** Bar-whisker plot of a percent difference in the E_{app} predictions between voxel-based FEA and geometry-based FEA, LEM and voxel-based FEA, and LEM and geometry-based FEA. At a significance level of 0.05, using repeated measures ANOVA, no statistical differences were observed among the E_{app} values derived from voxel-based FEA, geometry-based FEA, and LEM. Linear regression plots of the correlations between E^{LEM}_{app} and E^{FEA}_{app} for **(c)** bovine and **(d)** human samples. The dashed line corresponds to a one-to-one relationship between E^{LEM}_{app} and E^{FEA}_{app}. The equations of the regression lines (y = mx + b) with slopes (regression coefficients, m) and y-intercepts (b), and the coefficients of determination (R^2) are presented (slope p-value < 0.001 in all cases, intercept p-value > 0.2 in all cases, α = 0.05).

normalized to BV/TV was more closely correlated with the geometry-based FEA (R^2 = 0.92, slope p-value < 0.001) (Fig. 5b). A weak negative correlation was observed between the percentage difference in E_{app} and BV/TV between LEM and geometry-based FEA. No relationship was found between the percent difference of E_{app} and BV/TV between LEM and voxel-based FEA (Fig. 5c&d). In all cases, 95% of the data fell within the limits of agreement of Bland-Altman plots (±2 × standard deviation). On average, there was a constant bias of 24.0% between E_{app} predicted by LEM and voxel-based FEA of bovine bone cores (with the slope of the Bland-Altman regression not significantly different than zero); whereas, for the human bone cores, the bias was small (3.55%). LEM slightly over-predicted the E_{app} by 7.41% for bovine and 5.29% for human bone cores with respect to geometry-based FEA (Fig. 5e&f).

3.2. Convergence and performance analyses

LEM convergence analysis indicated LP = 0.12 mm was sufficient for accurate E_{app} predictions (supplemental material and Fig. 6). The difference between the firm and floppy boundary methods became negligible for 0.06 mm LP. Voxel- and geometry-based FEA mesh convergence analyses were performed for four of the human bone cores (9.00%, 11.2%, 17.8%, and 42.9% BV/TV). Convergence in E_{app} was achieved with a maximum edge length of 0.02–0.05 mm for voxel-based and 0.5–2.0 mm for geometry-based FEA.

To compare computational time between LAMMPS, Faim and Abaqus, all simulations were run on the same 14-core workstation. The wall time (CPU time divided by number CPUs) for LEM was similar to voxel-based FEA and less than the geometry-based FEA. As LP decreased in LEM, the simulation time increased (Table 1). The wall time solely considers the analysis performance and does not include the preparation time for input files.

4. Discussion

Patient-specific μFEA exhibits promising potential in fracture risk assessment, yet there remains a trade-off between speed, automation, and accuracy in using μFEA in pre-clinical and clinical settings. The novelty of this study was to introduce LEM as a potential alternative to μFEA for fast and accurate prediction of the mechanical behavior of trabecular bone cores. Bovine and human trabecular bone cores were analyzed from previous live bone experiments in which samples' geometry was purposely selected to maintain bone tissue viability for three weeks (Kunath, 2022; Meyer, 2016). Thus, the end- and side-effect artifacts (Ün et al., 2006) resulted in reduced E_{app} in contrast to specimens prepared for quantifying trabecular bone mechanical properties.

The E_{app} of bovine and human trabecular bone cores from voxel- and geometry-based FEA and LEM were compared. There were no statically significant (α = 0.05) differences between the E_{app} calculated from LEM and voxel- or geometry-based FEA. The E_{app} of bovine and human trabecular bone cores from LEM can accurately replicate E_{app} from voxel- and geometry-based FEA, showing a high degree of correlation (≥90%), which is similar to the result of a previous study where authors found a strong relation between E_{app} of a porous structure from FEA and LEM (Sun et al., 2022). Mayya et al. used a μCT-based spring network model of bovine trabecular bone and reported

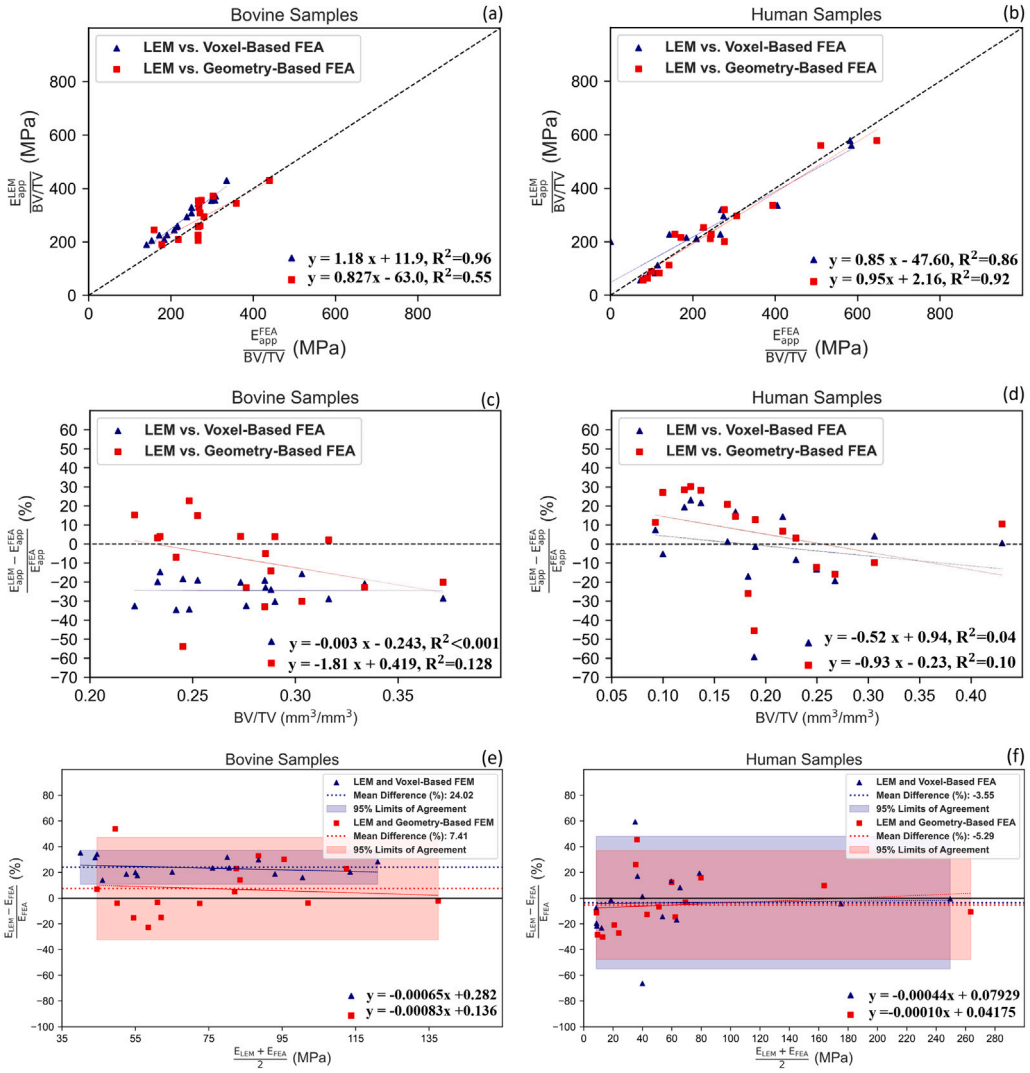

Fig. 5. Linear regression plots illustrating the proportional correlations for E_{app} and BV/TV between LEM and FEA of **(a)** bovine and **(b)** human bone cores, the black solid line shows zero percent difference. There was no relationship between the percent differences between E_{app}^{LEM} and E_{app}^{FEA} and BV/TV of μCT data of **(c)** bovine and **(d)** human samples. The dashed line corresponds to a zero percent difference between the E_{app}^{LEM} and E_{app}^{FEA}. Bland-Altman plots of **(e)** bovine and **(f)** human samples represent every difference between the two methods against the average of the estimations. An average bias of +24.0% and 7.41% between voxel- and geometry-based FEA and LEM for bovine samples was seen, while a small bias (<10%) between FEA and LEM in human samples was observed. The *y*-axis shows the difference percentage between the E_{app} from FEA and LEM, and the *x*-axis represents the average of these measures. The equations of the regression lines (y = mx + b) with slopes (regression coefficients, m) and y-intercepts (b), and the coefficients of determination (R^2) are presented. Slope p-value < 0.001 in all cases, intercept p-value > 0.2 in all cases. α = 0.05.

Table 1
Wall time required to perform FEA and LEM simulations is reported as a function of mesh size or lattice parameter. In all cases, 14 computer cores were employed. Results are shown for human bone core (ID #16).

Geometry-based FEA (ABAQUS)			Voxel-based FEA (Faim)			LEM				
Mesh size (mm)	Wall time (s)	E_{app} (MPa)	Mesh size (mm)	Wall time (s)	E_{app} (MPa)	LP (mm) simple cubic	Wall time (s) Firm boundary	Wall time (s) Floppy boundary	Total wall time (s) FFB	E_{app} (MPa)
0.1	3920	12.5	0.01	19 414	10.3	0.06	2936	1946	4882	11.0
0.5	1861	9.34	0.02	1045	9.25	0.08	263	198	561	9.58
1	1392	10.9	0.05	39	9.65	0.10	36	21	57	8.76
2	606	7.53	0.10	3	7.14	0.12	18	16	34	7.77

a strong correlation between experimental and numerical apparent linear stiffness (Mayya et al., 2016). To investigate the dependency of estimated E_{app} on trabecular bone porosity, a wide range of BV/TV (22%–38% for bovine and 9%–43% for human bone cores) was covered in this study. The correlation between E_{app} normalized to BV/TV from voxel-based FEA and LEM was strong (R^2 = 96% for bovine and R^2 = 86% for human bone cores). While the correlation between E_{app} normalized to BV/TV from geometry-based FEA and LEM was moderate (R^2 = 55%) for bovine bone cores, a strong correlation was found (R^2 = 92%) for human bone cores. This suggests a dependence of E_{app} on mesh density and BV/TV (Camacho et al., 1997). Given that the height of bovine samples was twice that of human samples, coarser meshes were generated for bovine bone cores in geometry-based FEA, resulting in an average of ~3.5 million elements in both bovine and human FEA. In general, the variation between geometry-based FEA and LEM was influenced by BV/TV and appeared as a random error. Despite the absence of a correlation between BV/TV and the percent difference between voxel-based FEA and LEM (R^2 < 5%), geometry-based FEA and

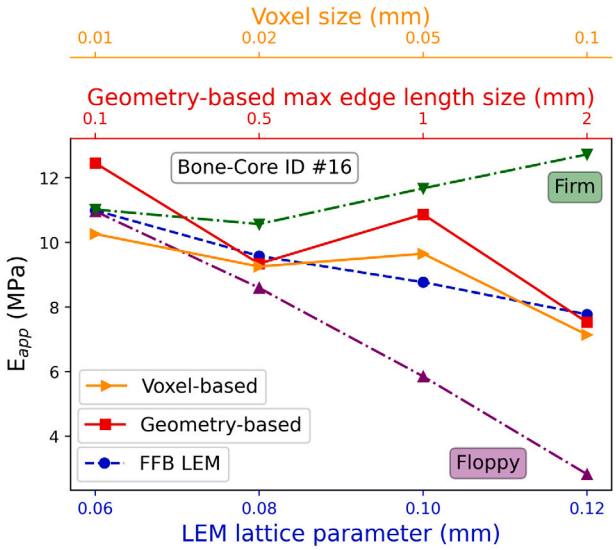

Fig. 6. Example of FEA and LEM convergence analyses of a human trabecular bone core (ID #16, 11.2% BV/TV). The FFB LEM E_{app} is the average of the firm and floppy boundary E_{app}.

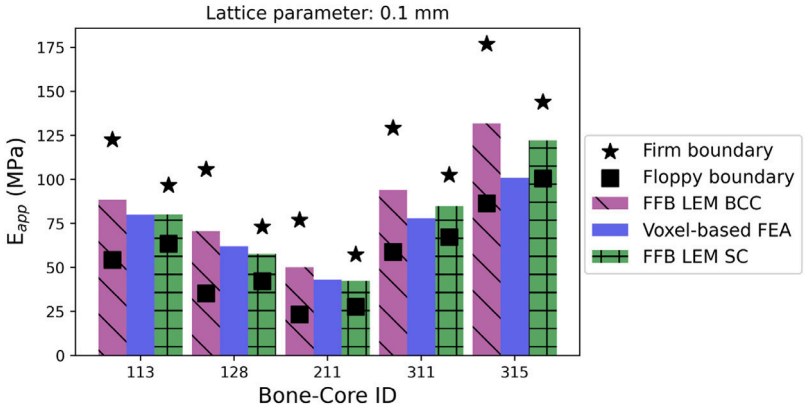

Fig. 7. E_{app} for five bovine bone cores calculated with FEA and LEM for both SC and BCC lattice structures with LP of 0.1 mm. The firm and floppy boundary E_{app} are shown with isolated star and square, respectively.

LEM were weakly correlated (R^2 = 13% for bovine and R^2 = 10% for human bone cores). The difference between geometry-based and LEM E_{app} was random. While LEM exhibited a bias of +24.0% compared to voxel-based FEA for bovine samples, a negligible random error (<5%) was shown for human samples. This indicates a systematic bias towards LEM for bovine trabecular bone cores characterized by higher BV/TV values.

Time to prepare simulations for LEM and voxel- and geometry-based μFEA were compared. Voxel conversion approach was faster than the tetrahedral meshing and eliminated user bias (Müller and Rüegsegger, 1995; van Rietbergen et al., 1995; Keyak, 2001). The total time for preparing voxel-based μFEA including image segmentation and preparing the input file for Faim (Windows, Intel(R) Xeon(R) W-2275 CPU @3.30 GHz, 14 core, 64 GB RAM), was between 10 min for the human bone cores with ~9.8 million nodes to 15 min for bovine bone cores with ~28.8 million nodes. Generating the quadratic tetrahedral mesh for the human bone cores with ~4.6 million nodes and ~6.1 million nodes for the bovine bone cores and input file generation for Abaqus (Windows, Intel(R) Xeon(R) W-2275 CPU @3.30 GHz 3.31GH, 14 core, 64 GB RAM) took almost an hour for both bovine and human bone cores. The main reason for using two different FEA solvers was that the voxel-based FEAs were too large to run efficiently in Abaqus. For LEM, the custom-made C code took about 10 min to build the input file for LEM for both firm and floppy boundary approaches. For LEM, the input files were prepared from the segmented μCT data without any modifications from the user. The only input variables in the C code were LP (in mm) and crystal structure (SC, BCC or FCC). The current version of C code is serial and it can become faster with parallelization. Additionally, the post-processing of firm boundary data with OVITO software should become automated in the future (Stukowski, 2009).

To test the effect of lattice structure, the E_{app} of five bovine bone cores, was also calculated employing a BCC lattice with 0.1 mm LP (Fig. 7). Similar E_{app} was found for LEM with SC or BCC lattice structures. The BCC structure took slightly more CPU time than SC. The difference was a few seconds for LP of 0.1 mm and increased for finer LPs. The increased time of BCC was due to more particles being present in the BCC structure (two particles per unit cell) in comparison with the SC one (one particle per unit cell) for a given LP. The SC had 18 bonds considering both the first and second nearest neighbors, while BCC had 14 total bonds per particle. Therefore, considering both the number of particles per unit cell and bonds per particle, BCC had more total bonds. Therefore the computational time for BCC was higher than SC lattice. Interestingly, the BCC structure respectively overestimated and underestimated the firm and floppy boundary E_{app} in comparison to SC. In the case of floppy boundary, SC led to a larger E_{app} because of a larger cut-off distance (LP×1.1) when building the input file in comparison with BCC ($\frac{\sqrt{3}}{2}$LP×1.1). This larger cut-off led to a slightly less porous structure in SC than BCC. In the case of the

firm boundary, the situation was reversed, due to the distance to the second nearest neighbor. This distance was smaller in BCC (1×LP) than SC ($\sqrt{2}$×LP) which decreased the number of particles considered in E_{app} calculations. Although BCC and FCC structures tend to perform and converge better than SC (Chen and Liu, 2016; Sun et al., 2022), the proposed FFB method performs better with SC structure.

5. Conclusions

FFB LAMMPS-LEM was introduced and assessed as an alternative to μFEA to predict the elastic response of trabecular bone in bovine and human bone cores. FFB LAMMPS-LEM required much less computer resources as compared to geometry-based FEA. In contrast, voxel-based FEA and FFB LAMMPS-LEM required similar computer resources and simulation time. All three methods led to consistent predictions of E_{app}, within statistical uncertainty. The benefit of FFB LAMMPS-LEM is that building the input simulation files based on segmented μCT data required minimal preparation and computer resources. Furthermore, FFB LAMMPS-LEM implementation has a computational cost that scales linearly with system size and allows for massive parallelism (Sun et al., 2022). In comparison, most FEA codes scale nonlinearly (N*log(N)) with the number of computer cores, N, and parallelism is typically limited to a few tens of computer cores.

Given FEA's maturity, extensive testing, and various FEA software package features, it will likely remain the best tool available in many biomechanical modeling scenarios. However, the current study showed that the LEM can offer a cost-accuracy ratio similar to that of FEA. Combined with other characteristics of particle-based methods, such as numerical stability under material failure scenarios, this points to further study and development of the FFB LAMMPS-LEM being warranted. Further investigations are underway to upgrade the LAMMPS-LEM to handle heterogeneous media, plastic deformation, and crack initiation and propagation.

Code availability

The in-house C code, additional source files for compiling LAMMPS, as well as examples of LAMMPS input scripts are available in the supplementary material.

CRediT authorship contribution statement

Mahsa Zojaji: Writing – review & editing, Writing – original draft, Software, Methodology, Investigation. **Keyvan Ferasat:** Writing – review & editing, Writing – original draft, Software, Methodology, Investigation. **McKinley Van Klei:** Methodology. **Hao Sun:** Software, Methodology. **Kail Beloglowka:** Methodology, Investigation. **Brian Kunath:** Methodology, Investigation. **Roshni Rainbow:** Writing – review & editing, Supervision, Funding acquisition. **Heidi-Lynn Ploeg:** Writing – review & editing, Writing – original draft, Validation, Supervision, Software, Project administration, Methodology, Investigation, Funding acquisition. **Laurent Karim Béland:** Writing – review & editing, Writing – original draft, Validation, Supervision, Software, Methodology, Investigation, Funding acquisition.

Declaration of competing interest

The authors declare that they have no known competing financial interests or personal relationships that could have appeared to influence the work reported in this paper.

Data availability

The data that support the findings of this study are available from the corresponding author upon reasonable request.

Declaration of Generative AI and AI-assisted technologies in the writing process

During the preparation of this work the authors did not use any AI and AI-assisted technologies in the writing process.

Acknowledgments

This work was financially supported by UNENE and NSERC (L.K.B.) and RGPIN/07210-2019 (H.P.). K.F., L.K.B. thank the Digital Research Alliance of Canada, formerly known as Compute Canada, for their generous allocation of computer resources.

Appendix A. Supplementary data

Supplementary material is available online through the portable document file (pdf) that includes the 2D illustration of firm and floppy boundary LEM, the convergence analysis of FFB LAMMPS-LEM, C code, and additional files for LAMMPS-LEM.

Supplementary material related to this article can be found online at https://doi.org/10.1016/j.jbiomech.2024.112209.

References

Adams, M.F., Bayraktar, H.H., Keaveny, T.M., Papadopoulos, P., 2004. Ultrascalable implicit finite element analyses in solid mechanics with over a half a billion degrees of freedom. In: SC'04: Proceedings of the 2004 ACM/IEEE Conference on Supercomputing. IEEE, p. 34.

Bardyn, T., Reyes, M., Larrea, X., Büchler, P., 2010. Influence of smoothing on voxel-based mesh accuracy in micro-finite element. In: Computational Biomechanics for Medicine. Springer, pp. 85–93.

Beloglowka, K., 2022. Ex vivo mechanical testing and FEA modelling of bovine trabecular bone.

Benca, E., Synek, A., Amini, M., Kainberger, F., Hirtler, L., Windhager, R., Mayr, W., Pahr, D.H., 2019. QCT-based finite element prediction of pathologic fractures in proximal femora with metastatic lesions. Sci. Rep. 9 (1), 10305.

Bland, J.M., Altman, D., 1986. Statistical methods for assessing agreement between two methods of clinical measurement. Lancet 327 (8476), 307–310.

Bott, K.N., Matheson, B.E., Smith, A.C., Tse, J.J., Boyd, S.K., Manske, S.L., 2023. Addressing challenges of opportunistic computed tomography bone mineral density analysis. Diagnostics 13 (15), 2572.

Boyd, S.K., Müller, R., 2006. Smooth surface meshing for automated finite element model generation from 3D image data. J. Biomech. 39 (7), 1287–1295.

Camacho, D.L., Hopper, R.H., Lin, G.M., Myers, B.S., 1997. An improved method for finite element mesh generation of geometrically complex structures with application to the skullbase. J. Biomech. 30 (10), 1067–1070.

Chen, H., Jiao, Y., Liu, Y., 2016. A nonlocal lattice particle model for fracture simulation of anisotropic materials. Composites B 90, 141–151.

Chen, H., Liu, Y., 2016. A non-local 3D lattice particle framework for elastic solids. Int. J. Solids Struct. 81, 411–420.

Depalle, B., Chapurlat, R., Walter-Le-Berre, H., Bou-Saïd, B., Follet, H., 2013. Finite element dependence of stress evaluation for human trabecular bone. J. Mech. Behav. Biomed. Mater. 18, 200–212.

Derikx, L.C., van Aken, J.B., Janssen, D., Snyers, A., van der Linden, Y.M., Verdonschot, N., Tanck, E., 2012. The assessment of the risk of fracture in femora with metastatic lesions: comparing case-specific finite element analyses with predictions by clinical experts. J. Bone Joint Surg. [Br] 94 (8), 1135–1142.

Derikx, L.C., Verdonschot, N., Tanck, E., 2015. Towards clinical application of biomechanical tools for the prediction of fracture risk in metastatic bone disease. J. Biomech. 48 (5), 761–766.

Dowhanik, S.P., Schieda, N., Patlas, M.N., Salehi, F., van der Pol, C.B., 2022. Doing more with less: CT and MRI utilization in Canada 2003–2019. Can. Assoc. Radiol. J. 73 (3), 592–594.

Du, X., Jin, L., Ma, G., 2014. Numerical modeling tensile failure behavior of concrete at mesoscale using extended finite element method. Int. J. Damage Mech. 23 (7), 872–898.

Flaig, C., 2012. A Highly Scalable Memory Efficient Multigrid Solver for μ-Finite Element Analyses (Ph.D. thesis). ETH Zurich.

Flaig, C., Arbenz, P., 2011. A scalable memory efficient multigrid solver for micro-finite element analyses based on CT images. Parallel Comput. 37 (12), 846–854.

Giavarina, D., 2015. Understanding bland altman analysis. Biochem. Med. 25 (2), 141–151.

Gislason, M.K., Ingvarsson, P., Gargiulo, P., Yngvason, S., Guðmundsdóttir, V., Knútsdóttir, S., Helgason, Þ., 2014. Finite element modelling of the femur bone of a subject suffering from motor neuron lesion subjected to electrical stimulation. Eur. J. Transl. Myol. 24 (3).

Guldberg, R., Hollister, S., Charras, G., 1998. The accuracy of digital image-based finite element models.
Keyak, J.H., 2001. Improved prediction of proximal femoral fracture load using nonlinear finite element models. Med. Eng. Phys. 23 (3), 165–173.
Knowles, N.K., Neeteson, N., Boyd, S.K., 2022. High performance multi-platform computing for large-scale image-based finite element modeling of bone. Comput. Methods Programs Biomed. 225, 107051.
Knowles, N.K., Whittier, D.E., Besler, B.A., Boyd, S.K., 2021. Proximal tibia bone stiffness and strength in HR-pQCT-and QCT-based finite element models. Ann. Biomed. Eng. 49 (9), 2389–2398.
Kunath, B.A., 2022. Design and validation of an open-source 3D printable bioreactor system for ex vivo bone culture.
Kunath, B.A., Beloglowka, K., Rainbow, R., Ploeg, H.-L., 2024. Mechanical loading of ex vivo bovine trabecular bone in 3D printed bioreactor chambers. J. Mech. Behav. Biomed. Mater. 106470.
Laubie, H., Monfared, S., Radjaï, F., Pellenq, R., Ulm, F.-J., 2017a. Effective potentials and elastic properties in the lattice-element method: Isotropy and transverse isotropy. J. Nanomech. Micromech. 7 (3), 04017007.
Laubie, H., Radjai, F., Pellenq, R., Ulm, F.-J., 2017b. A potential-of-mean-force approach for fracture mechanics of heterogeneous materials using the lattice element method. J. Mech. Phys. Solids 105, 116–130.
Laubie, H., Radjai, F., Pellenq, R., Ulm, F.-J., 2017c. Stress transmission and failure in disordered porous media. Phys. Rev. Lett. 119 (7), 075501.
Lin, E., Chen, H., Liu, Y., 2015. Finite element implementation of a non-local particle method for elasticity and fracture analysis. Finite Elem. Anal. Des. 93, 1–11.
Liu, X.S., Sajda, P., Saha, P.K., Wehrli, F.W., Guo, X.E., 2006. Quantification of the roles of trabecular microarchitecture and trabecular type in determining the elastic modulus of human trabecular bone. J. Bone Miner. Res. 21 (10), 1608–1617.
Mayya, A., Praveen, P., Banerjee, A., Rajesh, R., 2016. Splitting fracture in bovine bone using a porosity-based spring network model. J. R. Soc. Interface 13 (124), 20160809.
Meng, C., Wei, H., Chen, H., Liu, Y., 2021. Modeling plasticity of cubic crystals using a nonlocal lattice particle method. Comput. Methods Appl. Mech. Engrg. 385, 114069.
Mengoni, M., Sikora, S., d'Otreppe, V., Wilcox, R.K., Jones, A.C., 2016. In-silico models of trabecular bone: a sensitivity analysis perspective. Uncertain. Biol.: Comput. Model. Approach 393–423.
Meyer, L.A., 2016. Testing and Modeling Mechanical Properties of Ex Vivo Trabecular Bone (Ph.D. thesis). The University of Wisconsin-Madison.
Müller, R., Rüegsegger, P., 1995. Three-dimensional finite element modelling of non-invasively assessed trabecular bone structures. Med. Eng. Phys. 17 (2), 126–133.
Nikolić, M., Do, X.N., Ibrahimbegovic, A., Nikolić, Ž., 2018a. Crack propagation in dynamics by embedded strong discontinuity approach: Enhanced solid versus discrete lattice model. Comput. Methods Appl. Mech. Engrg. 340, 480–499.
Nikolic, M., Ibrahimbegovic, A., 2015. Rock mechanics model capable of representing initial heterogeneities and full set of 3D failure mechanisms. Comput. Methods Appl. Mech. Engrg. 290, 209–227.
Nikolić, M., Karavelić, E., Ibrahimbegovic, A., Miščević, P., 2018b. Lattice element models and their peculiarities. Arch. Comput. Methods Eng. 25, 753–784.
Nishiyama, K.K., Gilchrist, S., Guy, P., Cripton, P., Boyd, S.K., 2013. Proximal femur bone strength estimated by a computationally fast finite element analysis in a sideways fall configuration. J. Biomech. 46 (7), 1231–1236.
Ostoja-Starzewski, M., 2002. Lattice models in micromechanics. Appl. Mech. Rev. 55 (1), 35–60.
Palumbo, B.T., Nalley, C., Gaskins, III, R.B., Gutierrez, S., Alexander, III, G.E., Anijar, L., Nayak, A., Cheong, D., Santoni, B.G., 2014. Biomechanical analysis of impending femoral neck fractures: the role of percutaneous cement augmentation for osteolytic lesions. Clin. Biomech. 29 (3), 289–295.
Pericoli, V., Lao, X., Ziccarelli, A., Kanvinde, A., Deierlein, G., 2021. Integration of an adaptive cohesive zone and continuum ductile fracture model to simulate crack propagation in steel structures. Eng. Fract. Mech. 258, 108041.
Razi, S., Wang, X., Mehreganian, N., Tootkaboni, M., Louhghalam, A., 2023. Application of mean-force potential lattice element method to modeling complex structures. Int. J. Mech. Sci. 260, 108653.
Sas, A., Tanck, E., Sermon, A., van Lenthe, G.H., 2020. Finite element models for fracture prevention in patients with metastatic bone disease. A literature review. Bone Rep. 12, 100286.
Silling, S.A., 2000. Reformulation of elasticity theory for discontinuities and long-range forces. J. Mech. Phys. Solids 48 (1), 175–209.
Silling, S.A., Epton, M., Weckner, O., Xu, J., Askari, E., 2007. Peridynamic states and constitutive modeling. J. Elasticity 88, 151–184.
Srirekha, A., Bashetty, K., et al., 2010. Infinite to finite: an overview of finite element analysis. Indian J. Dent. Res. 21 (3), 425.
Stukowski, A., 2009. Visualization and analysis of atomistic simulation data with OVITO–the open visualization tool. Model. Simul. Mater. Sci. Eng. 18 (1), 015012.
Sun, H., Ferasat, K., Nowak, P., Gravelle, L., Gaffran, N., Anderson, C., Sirola, T., Pintar, O., Lievers, W.B., Kim, I.Y., et al., 2022. Implementing a non-local lattice particle method in the open-source large-scale atomic/molecular massively parallel simulator. Modelling Simul. Mater. Sci. Eng. 30 (5), 054001.
Taylor, M., Prendergast, P.J., 2015. Four decades of finite element analysis of orthopaedic devices: where are we now and what are the opportunities? J. Biomech. 48 (5), 767–778.
Taylor, W., Roland, E., Ploeg, H., Hertig, D., Klabunde, R., Warner, M., Hobatho, M., Rakotomanana, L., Clift, S., 2002. Determination of orthotropic bone elastic constants using FEA and modal analysis. J. Biomech. 35 (6), 767–773.
Thompson, A.P., Aktulga, H.M., Berger, R., Bolintineanu, D.S., Brown, W.M., Crozier, P.S., in't Veld, P.J., Kohlmeyer, A., Moore, S.G., Nguyen, T.D., et al., 2022. LAMMPS-a flexible simulation tool for particle-based materials modeling at the atomic, meso, and continuum scales. Comput. Phys. Comm. 271, 108171.
Ün, K., Bevill, G., Keaveny, T.M., 2006. The effects of side-artifacts on the elastic modulus of trabecular bone. J. Biomech. 39 (11), 1955–1963.
van Rietbergen, B., Weinans, H., Huiskes, R., Odgaard, A., 1995. A new method to determine trabecular bone elastic properties and loading using micromechanical finite-element models. J. Biomech. 28 (1), 69–81. http://dx.doi.org/10.1016/0021-9290(95)80008-5, URL https://www.sciencedirect.com/science/article/pii/0021929095800085.
van Rietbergen, B., Weinans, H., Huiskes, R., Polman, B., 1996. Computational strategies for iterative solutions of large FEM applications employing voxel data. Internat. J. Numer. Methods Engrg. 39 (16), 2743–2767.
Wang, X., Botshekan, M., Ulm, F.-J., Tootkaboni, M., Louhghalam, A., 2021. A hybrid potential of mean force approach for simulation of fracture in heterogeneous media. Comput. Methods Appl. Mech. Engrg. 386, 114084.
Wei, H., Chen, H., Liu, Y., 2020. A nonlocal lattice particle model for J2 plasticity. Internat. J. Numer. Methods Engrg. 121 (24), 5469–5489.
Zhou, X.-P., Tian, D.-L., 2021. A novel linear elastic constitutive model for continuum-kinematics-inspired peridynamics. Comput. Methods Appl. Mech. Engrg. 373, 113479.